Thermal Features of Lunar Regolith in Mare Humboldtianum based on Brightness Temperature Differences and Surface Parameters

Wei Cao[1,2], Zhiguo Meng[3], Aiju Li[4], Jietao Lei[3], Xuegang Dong[3], Ting Lan[5], Jiannan Zhao[6], Zhanchuan Cai[5], Binghua Su[1,2]

[1]School of Information Technology, Beijing Institute of Technology, Zhuhai, China; wcao@bitzh.edu.cn, bhsu@263.net
[2]Key Laboratory of Photoelectric Imaging Technology and System, Ministry of Education of China, Beijing Institute of Technology, Zhuhai, China; wcao@bitzh.edu.cn, bhsu@263.net
[3]College of Geoexploration Science and Technology, Jilin University, Changchun 130026, China; mengzg@jlu.edu.cn, leijt19@mails.jlu.edu.cn, dongxuegang69055@gmail. com
[4]Department of management and information, Shandong transport vocational college, China; ldtaiju@buu.edu.cn
[5]Faculty of Information Technology, Macau University of Science and Technology, Taipa, Macau; zccai@must.edu.mo
[6]Planetary Science Institute, China University of Geosciences, Wuhan, China; jnzhao@cug.edu.cn

Key Points:

- We map mulitchannel bright temperatures at multichannels 3GHz, 7.8GHz, 19.35GHz and 37GHz of the basaltic areas in Mare Humboldtianum, Moon.
- Most of the dTB anomalies show strong correlation with the special tectonic features.
- The BPNN correlation method shows the statistical result that most of dTB variations are related to roughness, curvature, and slope at different frequencies.

Corresponding author: Zhiguo Meng, `mengzg@jlu.edu.cn`

Abstract

Mare Humboldtianum is a Nectarian-aged basin on the northeast limb of the Moon, whose inner ring was flooded by basalt billions of years ago. The topography of Mare Humboldtianum is rather complex, which makes it difficult to define the basaltic units only by the spectral data. To improve understanding of the geological units in Mare Humboldtianum and provide new interpretations of the formation process, we use the brightness temperature (TB) data obtained by the Chang'E-2 (CE-2) mission, which is proved to have a good penetration feature. The TB difference (dTB) maps at multichannels are created to analyze the TB variations. The Backpropagation Neural Network (BPNN) model is first used to provide a statistical interpretation of the relation between dTB distributions and surface parameters. Our results show that, most of the dTB performances are strongly affected by the topography. Several abnormally dTB performances are observed on dTB maps. This observation indicates that there exists two different mare units in the eastern and western parts in the basin floor. These TB variations are interpreted that most of the dTB anomalies are strongly related to the special tectonic features. The statistical results based on BPNN method indicate that multichannel TB variations reflect different topographic features. Most of the topographic effects related to dTB variations are found in the regions controlled by the small craters and topographic bulges in the basin floor.

Plain Language Summary

The brightness temperature (TB) data collected by Chang'E-2 spacecraft provides an opportunity to study the thermal and dielectric properties of lunar regolith. Mare Humboldtianum exposes typical basalt materials, which can reflect the thermophysical features of the basin. In this paper, we evaluated the thermophysical features of Mare Humboldtianum based on the TB difference (dTB) maps at multichannels. The surface parameters are calculated to interpret the dTB distributions. We find that the dTB anomalies in the study region show strong correlation with the tectonic features. Compared with the surface parameters, dTB distributions reflect different topographic features at different frequencies.

1 Introduction

Mare Humboldtianum (Figure 1) is an Imbrian-age multiring basin located within Humboldtianum basin with a 650 km wide (Hiesinger et al., 1996). Typical ring terraces can be observed clearly in the digital terrain model with a grid spacing of 2 km and a height resolution of 500 m (Oberst et al., 1996). The inner ring of Mare Humboldtianum exposed extensive dark mare basalts (Moriarty & Pieters, 2016). Several smooth basalt exposures are presented in the area between the inner and outer basin rings. Both the central Mare Humboldtianum basalts and the inter-ring basalts exhibit a range in composition and age (Hiesinger et al., 1996, 2000). A basaltic composition is rich in high-Ca pyroxene based on the M3 target data with high spectral resolutions (Moriarty & Pieters, 2016). The basaltic volcanism of the basin center lasted longer than in the inter-ring area. The gravitational data from the Lunar Prospector spacecraft shows that Humboldtianum harbours a mass concentration (mascon) — a localized gravitational anomaly that tugs on orbiting spacecraft and suggests that the mascon is due to the presence of dense lunar mantle material lying within about 15 km of the surface (Booker et al., 1970; Freed et al., 2014).

The definition of homogeneous basaltic units is an important task to understand the nature and evolution of lunar basaltic volcanism (Hiesinger & Head, 2003; Hiesinger et al., 2010). For the geological unit definitions in Mare Humboldtianum, Hiesinger et al. (2000, 2011) provided the basaltic volcanism based on spectral data. The mare basalts in Mare Humboldtianum were therefore divided into 11 basalt units, where four units

were in the basin floor, called HU6, HU9, HU10, and HU11 (Figure 1). Moreover, Fortezzo et al. (2020) considered that two main geological units existed in the inner basalt area: Imbrian Upper Mare Units (Im2) and Imbrian/Nectarian Terra units (INt) . Im2 was caused by the basaltic lava flows and INt was the rolling terrain with complex formations by the erosional debris and basin ejecta. Other units, such as Lower Imbrian Mare Units (Im1) and Lower Imbrian Crater units (Ic1), also consisted of the topographies of the typical terrains and areas. Although the previous literatures provided significant definitions of basaltic units in Mare Humboldtianum, the crater deposits, wrinkle ridges, and mare basalts in the floor also affected the spatial distributions of geological units. To improve the understanding of the basalt units in the basin floor, Meng et al. (2018, 2019, 2020) showed that the Chang'E-2 microwave radiometer (CELMS) data could provide a way to improve the understanding of the definition of the mare geological units and the formation process of lunar basins.

Passive microwave remote sensing has been used to study the variations of lunar regolith properties (Zheng et al., 2012; Feng et al., 2020). The CELMS instrument worked at frequencies of 3, 7.8, 19.35 and 37GHz to obtain numerous data of lunar brightness temperature (TB) at 24 hours (Table. 1). These TB data are determined by the received solar energy and the thermal properties of the lunar regolith (Zheng et al., 2019). The 2C-level CELMS data with calibration are widely used in thermophysical feature analysis of Moon (Fang & Fa, 2014; Hu et al., 2015, 2018; Zhu et al., 2019). The latitude tendencies of the TB variations are obvious, which affect the evaluation of the basaltic units in the basin (Meng et al., 2020). Therefore, we create the TB difference (dTB) maps at 3, 7.8, 19.35, and 37GHz to improve the understanding of the thermophysical features of Mare Humboldtianum. dTB is defined as the TB differences between the TB data collected at noon and in the early morning (Meng et al., 2018, 2019, 2020).

Since the antenna footprints of CELMS data are 17.5 km (7.8, 19.35, and 37GHz) and 25 km (3GHz), the thermophysical features of the geological units smaller than the 17 km scale are difficult to understand. Therefore, some surface parameters are used to interpret the dTB variations at multichannels. Surface parameters are calculated for analyzing the geometrical properties of the surface (Olaya, 2009). In planetary surface analysis, surface parametrizations have been developed for a long time (Shepard et al., 2001; Kreslavsky & Head, 2000; Rosenburg et al., 2011; Kreslavsky et al., 2013; Cao et al., 2015; B. Li and X. Wang and J. Zhang and J. Chen and Z. Ling, 2016; Fa et al., 2016; Cao & Cai, 2018; Susorney et al., 2017, 2018, 2019; Cai & Fa, 2020). In this study, topographic roughness (Cao et al., 2018), Digital Terrain Entropy (DTE) (Lan et al., 2020), Slope, Aspectm, plane curvature (kh), and curvature (kv) (Li et al., 2017) are used for the correlation analysis of dTB variations. These parameters are calculated based on the SLDEM (Barker et al., 2016) and Lunar Orbit Laser Altimeter (LOLA) Gridded Data Records (GDRs) (Smith et al., 2010), which can be downloaded in `http://imbrium.mit.edu/`. Topographic roughness can provide 1 km-scale roughness textures for terrain analysis based on SLDEM. Other parameters can reflect 1.8 km-scale surface variations based on LOLA GDRs.

The paper is organized as follows. Section. 2 introduces the data processing and the details of the analyzed method. Section 3 provides a overview of the dTB maps of Mare Humboldtianum. Section 4 discusses the cause of the typical TB variations and analyzes the statistical correlations between dTB distributions and the surface parameters. The conclusion is stated in Section 5.

2 CELMS Data Processing and Surface Parameterizations

Since the latitude tendencies of TB data (Meng et al., 2018, 2019, 2020), dTB maps are created to reduce this effect in thermal feature analysis of Mare Humboldtianum. Moreover, high-resolution Digital Elevation Models (DEMs) of lunar topography can provide

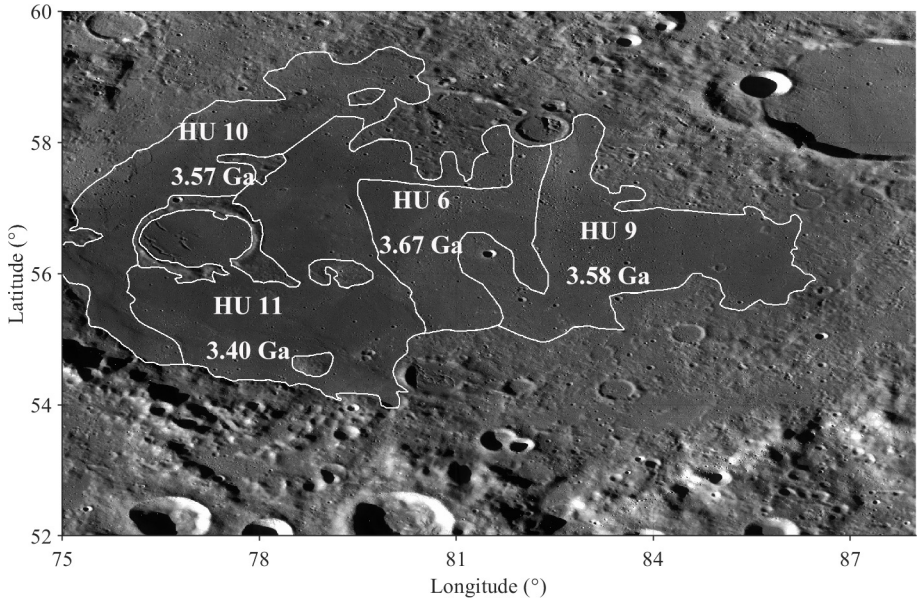

Figure 1: Basaltic units of Mare Humboldtianum. The geological boundaries are created based on the results in Hiesinger and Head (2003). The model ages of these geological regions were estimated by Hiesinger et al. (2011) (Unit: Ga). The base map is the LRO WAC image, which is derived from the Quickmap (`https://quickmap.lroc.asu.edu/`).

abundant topographic information for the identification and characterization of craters, basins and important data for understanding the impact process and history, thermal evolution, large events of lunar surface (Head et al., 2010; Baker et al., 2012; Fassett et al., 2012). Therefore, some surface parameters are used for thermophysical feature analysis indicated by dTB distributions based on the lunar high-resolution DEMs. Topographic roughness shows the 1 km-scale textural map to interpret the dTB distributions. Other surface parameters are used for correlation analysis with multichannel dTB values.

2.1 TB Difference (dTB) Maps

The CELMS data are collected by the microwave radiometer onboard the Chang'E-2 (CE-2) spacecrafts. The antenna footprint of CE-2 MRM is 17.5 km for 7.8, 19.35, and 37 GHz channels, and 25 km for 3GHz (Lan & Cai, 2018). The CELMS data in 2C level are collected by CE-2 satellite from October 2010 to June 2011. The 2C-level CELMS data are the raw TB data with geometric correction and radiometric calibration (Fang & Fa, 2014; Hu et al., 2018). These data are widely used for studying microwave thermal emission features (Lan & Cai, 2018; Zhu et al., 2019; Meng et al., 2020). In this study, we use the 2C-level CELMS data as the source data.

To reduce the effect of TB latitude tendencies, we create the dTB maps at 3, 7.8, 19.35, and 37GHz. Based on the comparison of the TB distributions at every hour (Figure 2), the TB data at 11 and 13 o'clock for noon, and 2 and 4 o'clock for early morning are better to generate the dTB maps. Since the number of TB data is not enough to cover the whole area of Mare Humboldtianum, the raw data are gridded by the linear interpolation (Meng et al., 2018, 2019).

The TB differences (dTB) between noon TB and night TB at the same frequencies is directly related to the regolith thermophysical parameters within the penetration depth of the corresponding microwave data (Meng et al., 2019, 2020). Since the TB points

Table 1: The number of global TB data at one day (24 hours)

Hour	The Number of TB Points[a]
0	321724
1	520454
2	514494
3	363131
4	327261
5	337407
6	337400
7	333915
8	315842
9	304989
10	282362
11	272508
12	319624
13	521174
14	520532
15	368434
16	338646
17	345198
18	344377
19	333046
20	318199
21	309892
22	287008
23	272867

[a] the numbers of TB data with different frequencies at one hour are the same.

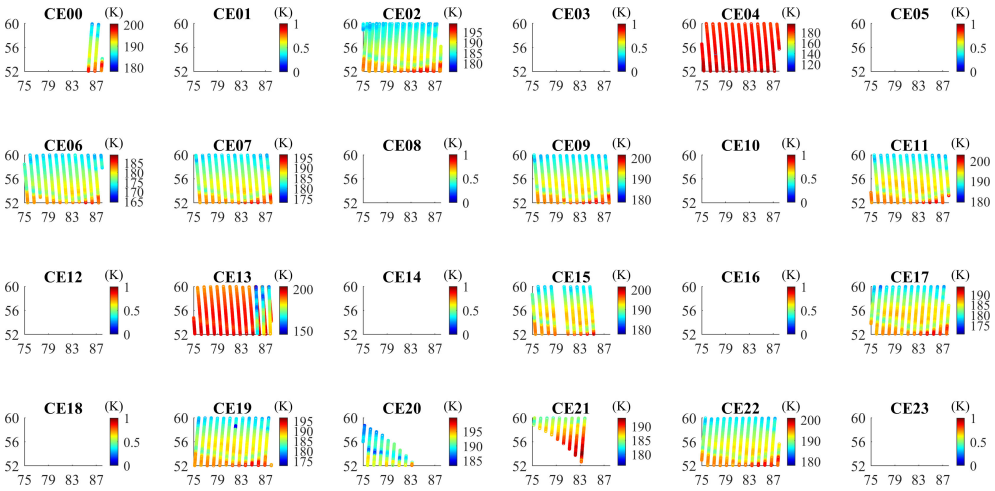

Figure 2: The raw TB data of Mare Humboldtianum at 24 hours, where x-axis and y-axis denote the longitudes and latitudes, respectively. The titles CE01-23 denote the hours. The data at 2, 4, 11 and 13 o'clock provide better qualities and enough points for TB map generation.

are scattered in the latitude-longitude coordinate system, the scattered TB points are interpolated by the triangulation-based linear interpolation. All the interpolated points

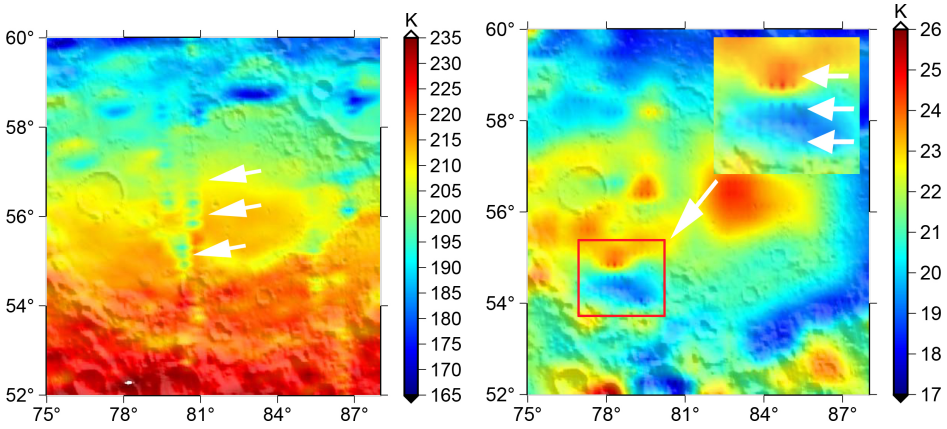

(a) TB at 13 o'clock (b) dTB based on 2 and 11 o'clocks

Figure 3: The TB and dTB abnormal values: (a) The abnormal TB values along latitudes; (b) dTB abnormal values based on the TB data at 2 and 11 o'clocks. White arrows point to these abnormal values on the maps. Red circle denotes the abnormal dTB values on the maps.

are located inside the convex hull of the original data points. Some interpolated points at the edges are defined as NaN values. To solve this problem, the interpolated latitudes and longitude values (La and Lo) are expressed as follows:

$$La = [max(la) - min(la) + 4] * a \tag{1}$$

$$Lo = [max(lo) - min(lo) + 4] * a \tag{2}$$

where la and lo denote the original latitude and longitude value, respectively. The value 4 means that additional four original points are used in the interpolation to remove the effect of NaN values. The redundant interpolated points at the edges are deleted after the interpolation. a denotes the interpolated points for one degree. Therefore, the interpolated TB values can be expressed as follows:

$$TB_{time} = linear(La, Lo, (la, lo, rTB)) \tag{3}$$

where $time$ denotes the local hour in Table 1. The function $linear$ denotes the linear $griddate$ function in MATLAB software. The linear function are fitted by the raw data (la, lo, rTB), where rTB denotes the TB values of CE-2 2C-Level data.

The interpolated TB maps have resolutions of $0.25° \times 0.25°$. The dTB maps (3GHz, 7.8GHz, 19.35GHz, and 37GHz) can be expressed as:

$$dTB = TB_n - TB_m \tag{4}$$

where TB_n and TB_m denote the interpolated TB maps at noon and in the early morning, respectively.

To provide the reasonable observations of dTB variations, we test the TB data at 2, 4, 11, 13 o'clocks by creating their TB or dTB maps. At the channel 19.35GHz, we find some abnormal data in the TB data at 13 o'clock and dTB map based on TB data at 2 and 11 o'clocks. As shown in Figure 3, the abnormal TB data at 13 o'clock can be observed along the latitudes nearby 81°E (Figure 3(a)). In Figure 3(b), the dTB maps based on the TB data at 2 and 11 o'clock show some abnormal TB data along the latitudes (large window with three white arrows). Therefore, we select the TB data at 4 and 11 o'clock to create the multichannel dTB maps (Figure 4).

2.2 Surface Parameterizations

In this study, topographic roughness calculated in Cao et al. (2018) can quantify the amplitude of topographic features of elevations at a horizontal scale. The roughness values are expressed as:

$$R(\frac{M}{2},\frac{M}{2}) = \frac{1}{M \times M}\left(\sum_{x=1}^{n}\sum_{y=1}^{n} M_{matrix}\left(x,y\right) Z\left(y,x\right) M_{matrix}^{T}\left(x,y\right)\right) \tag{5}$$

where M is the number of pixels in the moving window. M_{matrix} denotes the V-system matrix created by the V-system series (Song et al., 2007). R denotes the parametrized value of roughness centred at the scale (defined as a moving window with size of $M\times M$). Z is the DEM determined by the $M\times M$ moving window. x and y denote the latitude and longitude, respectively.

DTE (Lan et al., 2020) is a surface parameter used to reflect the quantity of the geomorphic information obtained in the DEMs:

$$DTE = -\sum\sum plog_2 p \tag{6}$$

where p denotes the the ratio of the elevation value of a local point on lunar surface.

Other parameters are provided by Li et al. (2017). The calculations of these parameters are given as follows.

Slope is defined as the elevation variability of lunar topography, which can be expressed as follows:

$$Slope = arctan\sqrt{F_x^2 + F_y^2} \times 180^\circ/\pi \tag{7}$$

where F_x^2 and F_y^2 denote the elevation change rates in the longitude and latitude, respectively.

Aspectm can determine the amount of solar radiation, which influences local site microclimate (Ahmadzadeh & Petrou, 2001). In this study, Aspectm is defined as the ratio of the given pixel at the longitude x and latitude y:

$$Aspectm = arctan(F_y^2/F_x^2) \tag{8}$$

where F_x^2 and F_y^2 are the same as those in Equation. 7.

Curvature provides a quantitative measurement to quantify the pixels' distortion degree of DEMs. In this study, the curvatures calculated by the pixels at horizontal and vertical directions are called plane curvature (k_h) and section curvature (k_v), respectively. The expressions of these parameters are given as follows:

$$k_v = -\frac{p^2r + 2pqs + q^2t}{(p^2+q^2)\sqrt{1+p^2+q^2}} \tag{9}$$

$$k_h = -\frac{q^2r + 2pqs + p^2t}{(p^2+q^2)\sqrt{1+p^2+q^2}} \tag{10}$$

where p, q, r, s, and t can be expressed based on the local DEM z (Li et al., 2017):

$$p = \frac{\partial z}{\partial x}, q = \frac{\partial z}{\partial y}, r = \frac{\partial^2 z}{\partial^2 x}, s = \frac{\partial^2 z}{\partial x \partial y}, t = \frac{\partial^2 z}{\partial^2 y} \tag{11}$$

where x and y denote the longitude and latitude, respectively.

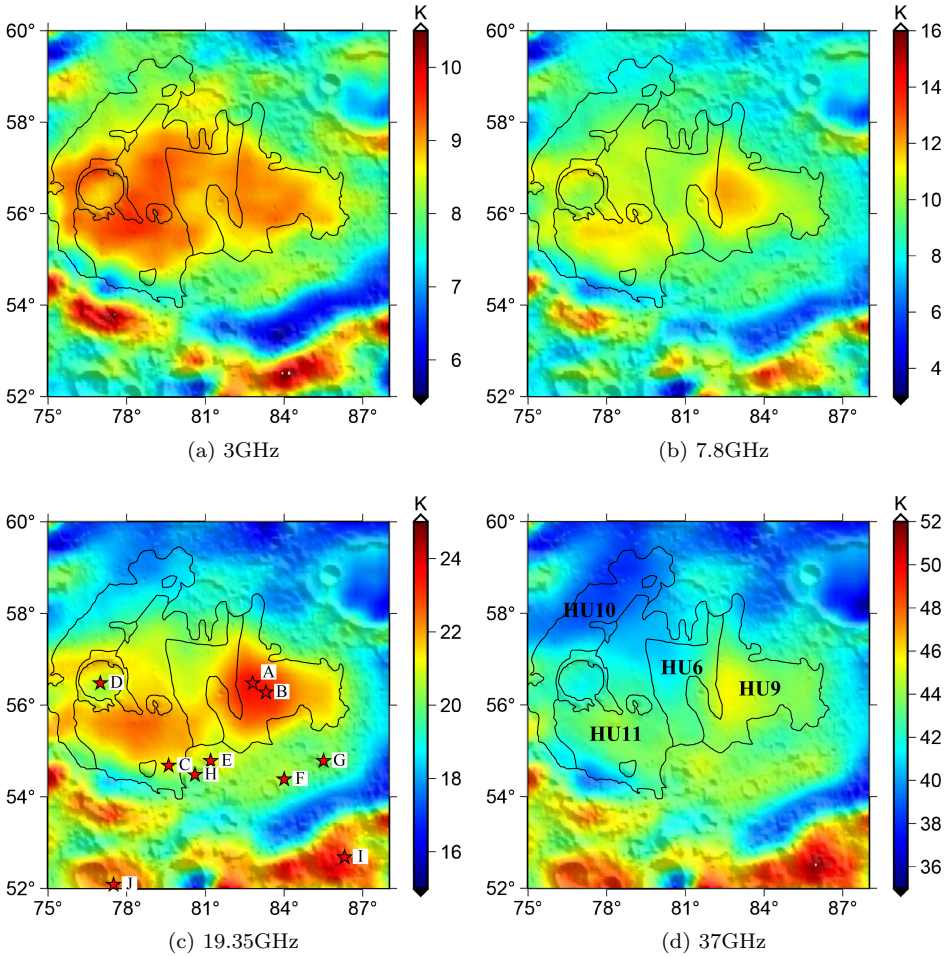

(a) 3GHz (b) 7.8GHz

(c) 19.35GHz (d) 37GHz

Figure 4: Multichannel dTB gridded maps created based on the TB data at 4 and 11 o'clock. Black lines denote the geological boundary marked in Figure 1. The points in (c) show typical dTB performances, where A: (82.8°E, 56.5°N); B: (83.3°E, 56.3°N); C: (79.6°E, 54.7°N); D: (77°E, 56.5°N); E: (81.2°E, 54.8°N); F: (84°E, 54.4°N); G: (85.5°E, 54.8°N); H: (80.6°E, 54.5°N); I: (86.3°E, 52.7°N); J: (77.5°E, 52.1°N). The names of defined units are marked in (d).

3 Results

3.1 Multichannel dTB maps

Figure 4 shows the dTB maps at 3, 7.8, 19.35, and 37GHz. The related histograms of dTB values are given in Figure 5. The geological boundaries (Hiesinger & Head, 2003; Hiesinger et al., 2011) are marked in the figures. At 19.35GHz (Figure 4(c)), we mark some typical dTB variations on the maps for thermophysical feature analysis of mare deposits and the names of defined units are shown in Figure 4(d). As a systematic overview, the dTB values become larger following with the frequency increases. The dTB performances in the western part of the basin floor are complex. At 3.0 GHz, the dTB here is similar as that in the eastern part. But from 7.8 GHz, the dTB in the western part is clearly lower than that in the eastern part. Particularly, at 37 GHz, the dTB is similar to the extensive regions in the Basin floor, which is about 2 K lower than that in the

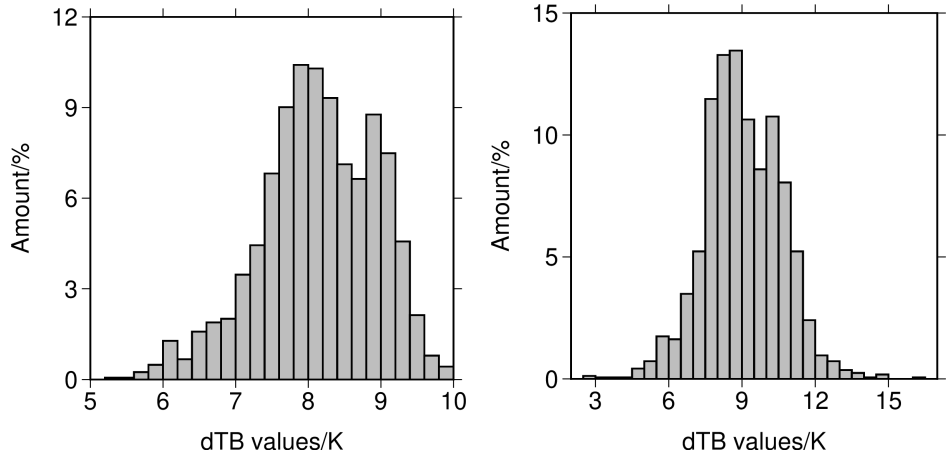

(a) 3GHz (b) 7.8GHz

(c) 19.35GHz (d) 37GHz

Figure 5: The histograms of dTB values at (a) 3GHz; (b) 7.8GHz; (c) 19.35GHz; (d)37GHz.

eastern part. More details of the dTB distributions at each channel are provided as follows:

At 3GHz (Figure 4(a)), dTB values varies from 5.4 to 10.9 K. The interval of histogram bin boundaries is 0.2 (Figure 5(a)). Three clusters of high dTB distributions ($\geq$ 10) can be observed in HU6, HU9, HU10, and HU11. The cluster with highest values is clearly realated to the regions covered by the mare basalts, while the area is smaller than those indicated by the optical data. The clueset with lowest values is clearly related to the regions in the southern part of HU11, which is likely brought by the low volumetric temperature for the topography opposite to the solar illumination (Meng et al., 2019). And the rest regions are responsible for the cluster with middle values.

At 7.8GHz (Figure 4(b)), the dTB varies from 2.7 to 16.9 K. The interval of histogram bin boundaries is 0.5 (Figure 5(b)). Most of the obvious high dTB values are appeared in the western part of HU9, and other parts can be seen in HU6. HU10 also shows high dTB distributions ($\geq$ 12), which are in the south of the crater (centered at point D). Three clusters of high dTB distributions ($\geq$ 10) can also be observed in HU6, HU9, HU10, and HU11. The cluster with highest values is much smaller than that at 3.0 GHz,

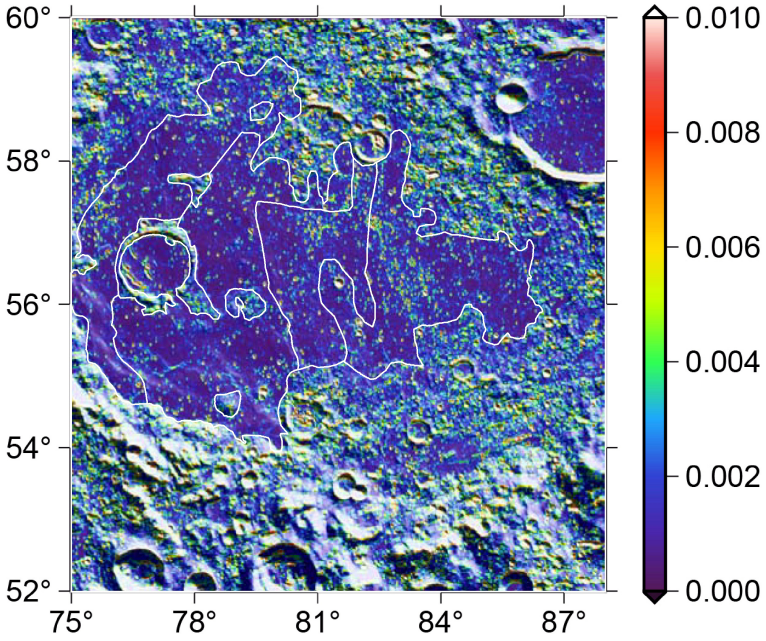

(a) 1km-scale Roughness

Figure 6: Topographic roughness map created by Cao et al. (2018). The white lines denote the geological boundaries marked in Figure 1.

which is related to two small patches centered at Point A and at the northwest place of Point C. The clueser with lowest values is clearly related to the regions in the northern part of HU10 and the southern part of HU11. And the rest regions are responsible for the cluster with middle values, which is extensively distributed in the Mare floor.

At 19.35GHz (Figure 4(c)), the interval of dTB differences become larger (from 15.1 to 25.0 K). The interval of histogram bin boundaries is 0.5 (Figure 5(c)). Mass high dTB distributions ($\geq$ 22) are local in HU9 and HU11. A cluster of dTB distributions ($\geq$ 22), which is appeared in the southern part of HU6, "connects" the high dTB distributions in HU9 and HU11. Two dTB clusters can be observed in HU6, HU9, HU10, and HU11. The cluster with higher values is related to two small patches centered at Point A and at the northwest place of Point C. The cluster with lower values is clearly related to the regions in the northern parts of Hu6, 10 and 11.

At 37GHz (Figure 4(d)), the range of dTB changes is from 34.6 to 52.5 K. The interval of histogram bin boundaries is 0.5 (Figure 5(d)). Most of dTB variations ($\geq$ 46) are local in the western part of HU9. Four clusters of high dTB distributions ($\geq$ 44) can be observed in HU10, HU11, and HU9, HU6. The cluster with highest values is related to patch centered at Point A. The cluster with second highest values is related to the patch centered at the northwest place of Point C. The clueser with lowest values is clearly related to the regions in the northern part of Hu6, HU10, HU11 and the southern part of HU11. Such dTB performances at different frequency also hint a good description of the change of the regolith thermophysical features with depth.

In conclude, The dTB values in HU9 and HU11 show most of the high dTB distributions at multichannels. These dTB distributions show different result from the unit definition in Hiesinger et al. (2011).

3.2 Topographic roughness map

The 1 km-scale topographic roughness (Cao et al., 2018) is mapped to analyze the topographic features related to typical dTB variations (Figure 6). As a systematic overview, topographic roughness cannot show obvious linear relationships to the dTB variations. High roughness textures (green to yellow colorshades, from 0.004 to 0.006 in Figure 6) caused by the small craters in HU9, the edges of the bulge in HU11, and the crater rims centered at point D. In HU9, high roughness variations can be seen the area centered at point A (Figure 4(a)-(d)) and caused by the small craters. The cluster of these craters indicates high roughness distributions with banded structures. Some high roughness textures distribute near the topographic bulges and in the small craters at the south parts of HU11. Other high roughness textures appear in the crater rims centered at point D. The low roughness values are caused by the smooth and young mare basalts (Figure 1).

As a systematic overview, the roughness textures in the units defined in Hiesinger et al. (2011) cannot show similar or homogeneous textural variations and distributions. Small craters, deposits on crater rims and topographic buldges cause the high roughness values. Compared with the dTB distributions (Figure 4), high dTB regions (HU9 and HU11) indicate different roughness features. In HU9, the scattered roughness textures are mainly caused by the northern small crater. The scattered textural variations are from northwestern to southern parts of HU9. These roughness variations are related to the high dTB variations in Figure 4(d), because dTB values decrease from western to eastern parts of HU9. In HU11, high dTB values can be observed near the crater rim (Figure 4). The roughness textures indicate two high linear distributions, which are caused by the small craters and topographic bulges (Figure 1), from southwestern to northeastern parts of HU11. High dTB distributions can be seen in the region between the two linear roughness textures, and are related to low roughness textures.

Thus, the roughness textures show a different unit distributions from the previous results (Hiesinger & Head, 2003; Hiesinger et al., 2011). Moreover, high roughness textures indicate that high dTB distributions are mainly related to the scattered topographic variations caused by small craters and topographic bulges.

4 Discussions

4.1 Re-evaluation of mare basalt units

In this part, we provide the analysis of dTB distributions to show that: (1) the visible data is not rational to reflect thermophysical features in the study area; (2) dTB performances can indicate new descriptions about basaltic units and related volcanic activities.

Hiesinger et al. (2011) subdivided the western part into HU10 unit aged 3.57 Ga in the western part and HU11 unit aged 3.40 Ga in the eastern part. However, the difference between the two units is not clearly in the dTB maps. Therefore, the geologic units identified only with visible data should be severely treated. Moreover, Figure 7 shows that the FTCs in the southern part are higher than those in the northern part. Correspondingly, the dTB in the former is apparently higher than that in the latter, validating the strong correlation between the FTCs and the dTB values. Figure 4 indicates that there exists a bad correspondence between the dTB performances and the basaltic units (Hiesinger & Head, 2003; Hiesinger et al., 2011). Figure 8 indicates the histograms of dTB values in the defined basaltic units. Theoretically, each peak in the histogram denotes one type of basalt units. HU6 can show four types of basaltic units at multichannels (Figure 8(a)). However, there are only three types of basalt units shown in HU9 (Figure 8(b)), HU10 (Figure 8(c)), and HU11 (Figure 8(d)), which are clearly related to the dTB in the basin floor (relatively higher values), the region surrounding the basin floor, and the nearby highlands (relatively lower values) as mentioned in Section 3. That is,

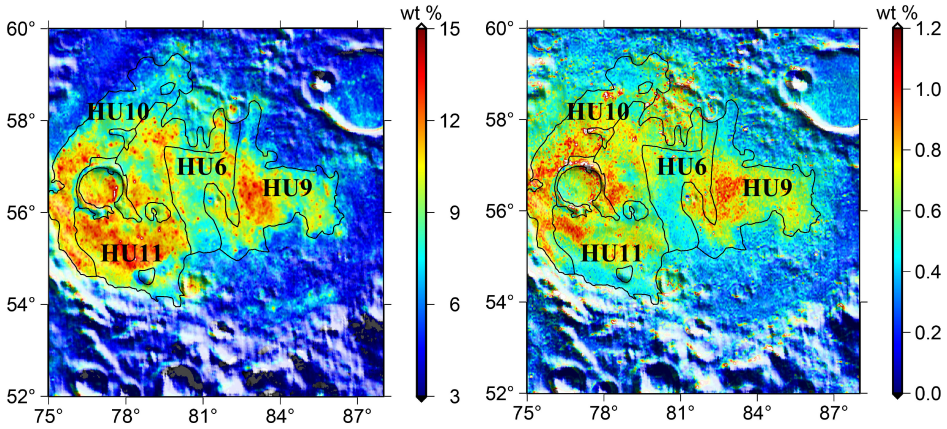

(a) FeO (b) TiO_2

Figure 7: FeO and TiO_2 contents (FTCs) used for TB analysis. (a) FeO; (b) TiO_2. The black lines denote the geological boundaries marked in Figure 1.

the previous division of the basalt units only by visible data is not rational to reflect the thermophysical features of the mare units.

According to the previous studies of the mare basalts with CELMS data (Meng et al., 2018, 2019, 2020), the high dTB is probably related to the high FeO+TiO_2 contents (FTCs) of the mare deposits. Therefore, the FTCs estimated with the Clementine UV-VIS data using the Lucey method are employed in this study (Figure 7). Figure 4 postulates that the dTB can mainly be divided into three categories. The first category is the basin center with the highest dTB. The dTB performances in this category are apparently dominated by the FTCs (Figure 7(a) and (b)). The second category is the northern part of units HU6 and HU10, where the dTB and the FTCs are clearly lower than the remanet part of the mare places. The third category is the the northern and southern rims of the Humbolditanium, which indicates the second lowest and highest dTB values, respectively. Considering the deficient solar illumination in the northern part and the enhanced solar illumination in the southern part of the Basin wall, the dTB performances here are highly related to the topography opposite to the solar illumination. That is, the dTB performances in the study area should be strongly affected by the topography. Interestingly, we mentioned that the relatively larger craters in the basin floor, the dTB is similar surrounding the craters wall, indicating that the influence of the topography on the dTB is limited. Moreover, the dTB performances show a fairly strong correlation with the FTCs (Figure 7(a) and (b)), indicating that the FTC is the dominated factor of the dTB. Thus, the dTB maps imply a good description of the basaltic units in the study area.

Generally, the dTB performances indicate a new description about the basaltic volcanism in Mare Humboldtianum. At first, the geologic boundaries interpreted by Hiesinger et al. (2011) are not identified by the dTB performances. But according to the dTB performances, the mare basalts can be subdivided into the eastern and western parts in the Basin floor. The difference between the optical result and the microwave result is likely brought by the strong contamination of the ejecta from the faraway places. Secondly, in this small time range, the youngest basalt should be in the eastern part of the Basin floor, where the highest dTB values imply that the FTCs should be much higher than those in the western part. Especially, we mentioned that the apparent distribution of the ejecta in the eastern unit. Moreover, the craters distributed in boundary lines also indicate the strong influence of the ejecta from the faraway places. That is, the eastern

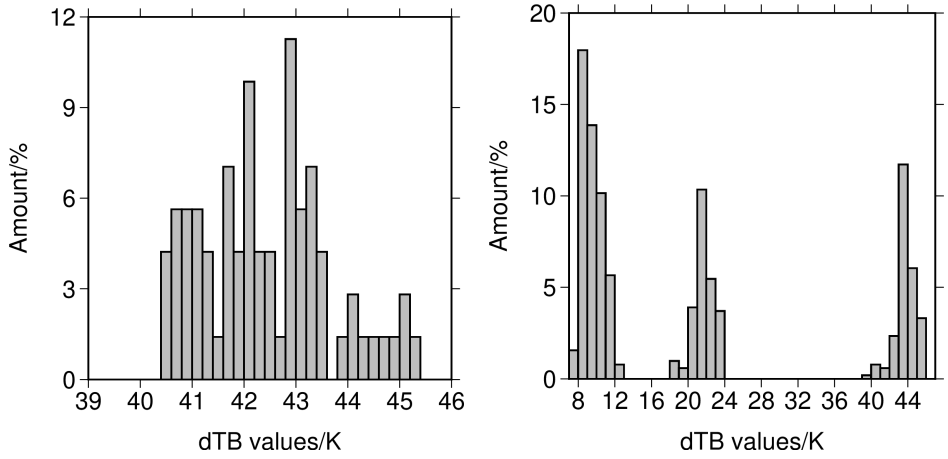

(a) HU6 (b) HU9

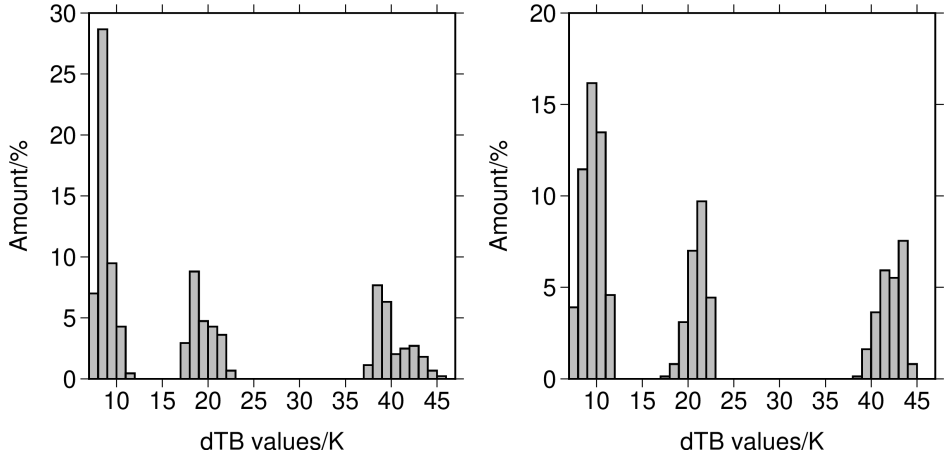

(c) HU10 (d) HU11

Figure 8: The histograms of dTB values of the defined geological units (HU6, HU9, HU10, and HU11) in Mare Humboldtianum (Hiesinger et al., 2011) at multichannels (3, 7.8, 19.35, and 37GHz). Each histogram contains all the dTB values of the defined geological units at the selected channels.

region with high dTB anomaly should be strongly altered by the impact ejecta in the surface layer, which decreased the surface FTCs and elevated the calculated surface age. Thus, what we found about the basaltic volcanism should be rational according to the microwave radiometer data with considerable penetration ability.

4.2 dTB Anomaly

Figure 4(c) indicates that there exits an abnormally high dTB zone centered at point A (82.8°E, 56.5°N) in the eastern part of the Basin floor. Here, high dTB anomaly is about 85 km × 55 km at 3.0 GHz, which is about 2 K evenly higher than its east vicinity. The anomaly keeps constant at 7.8 and 19.35 GHz, while there occurs a small patch with highest dTB centered at point A (82.8°E, 56.5°N) with a 15-km diameter at 7.8 GHz and it extends to the 30-km diameter at 19.35 GHz. At 37 GHz, the high dTB anomaly decreases to a smaller patch centered at point A (82.8E, 56.5N) with the size of 35 km × 45 km, which is also about 2 K higher than its vicinity.

What brought the high dTB anomaly? No wrinkle range or apparent cones are found in this zone. Although there exist abundant relatively smaller craters, the distribution of the dTB values is not related to the craters distribution. Interestingly, Figure 4(c) shows that there is a zone with relatively higher FTCs centered at point B (83.3°E, 56.3°N), and the FTCs largely agree with the highest dTB anomaly at 19.35 GHz, indicating that strongly correlation between the dTB and the FTCs. Therefore, the high dTB anomaly should be attributed to the high FTCs.

Hiesinger and Head (2003) categorized this region into HU6 unit aged 3.67 Ga in the western part and HU9 unit aged 3.58 Ga in the eastern part. However, the boundaries are not identified by the dTB maps, which indicates the evenly high values in the two units. Moreover, the FTCs show that the dTB in the middle-western part of the Basin floor (HU11 unit defined by Hiesinger et al. (2011)) are apparently higher than those in the place with high dTB anomaly, while the dTB in the former is similar to the latter at 3.0 GHz and it is much lower than that in the latter at the other three channels. Meng et al. (2018, 2019, 2020) proposed that the dTB is strongly correlated to the FTCs, and the regions with higher FTCs have higher dTB values. Thus, the FTCs of the lunar regolith the region with high dTB anomaly should be higher than those in HU11 unit. But Figure 4 presents a different view about the aforementioned conclusion, where the FTCs of the lunar regolith the region with high dTB anomaly are lower than those in HU11 unit. There occurs several abnormally high dTB performances besides that in the eastern part of the basin floor (Figure 4(c)):

The first one is located in the southern part of HU11 unit (Figure 1). The anomaly is extended from the crater centered at point C (79.6°E, 54.7°N) to the southeast rim of a crater centered at point D (77.0°E, 56.5°N). Here, the dTB is similar as its vicinity at 3.0, 7.8, and 19.35 GHz, but it is apparently higher than its vicinity at 37 GHz. The FTC maps (Figure 7(a) and (b)) present the high FTCs in this region, but the distribution of the high dTB anomaly does not agree with the FTC maps.

The second to fourth anomalies are located in the places centered at point E (81.2°E, 54.8°N), point F (84.0°E, 54.4°N), and point G (85.5E, 54.8N), which are clearly not related to the topography. There exist abundant surface fractures in the crater point H (80.6°E, 54.5°N) near the site at point E (81.2E, 54.8N). Moreover, a clear depression occurs in the northeast part of the crater centered at point H (80.6°E, 54.5°N), indicating the ever-existed strong tectonic activities in this site.

The fifth and sixth anomalies are located in the places centered at point I (86.3°E, 52.7°N) and point J (77.5°E, 52.1°N), the southern wall beyond the basin floor. However, both the FTCs do not support the high dTB anomalies. We mentioned that the crater density is fairly high in the fifth anomaly. Moreover, a probably rille is just in the east part. Additionally, there occurs a small patch with relatively smooth surface with lower topography in the sixth anomaly.

380 ### 4.3 Correlation analysis of TB distributions

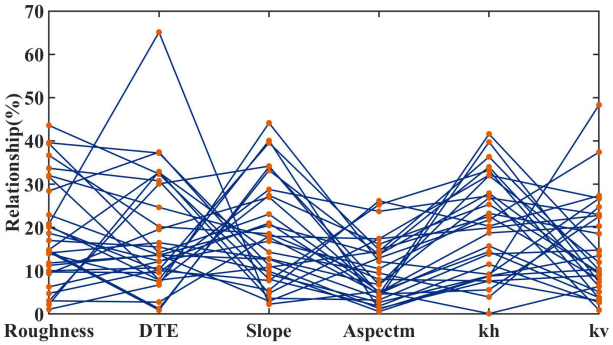

(a) 3GHz

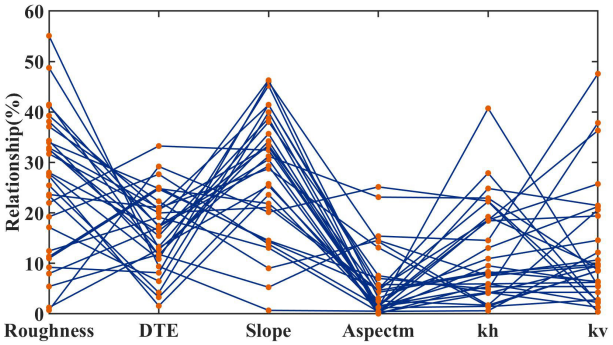

(b) 7.8GHz

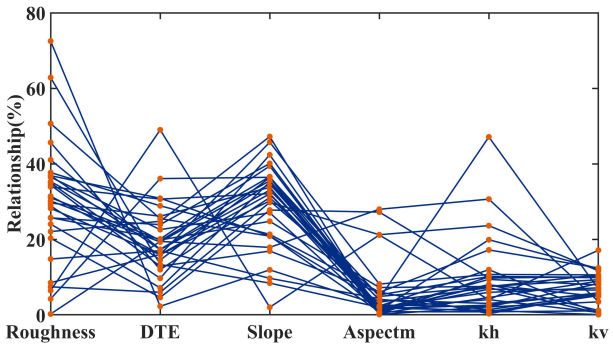

(c) 19.35GHz

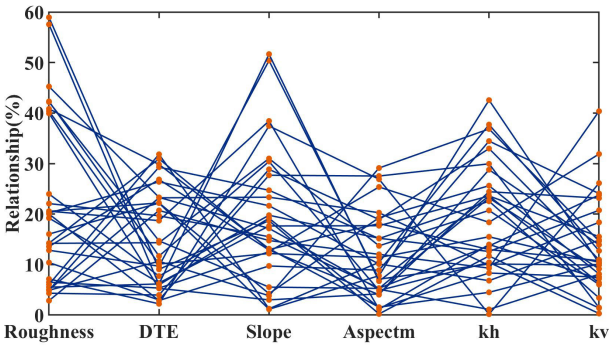

(d) 37GHz

Figure 9: Correlation analysis of dTB values and surface parameters based on BPNN method (Li et al., 2017). Most of the dTB values are related to DTE (Lan et al., 2020) at 3GHz, Slope at 7.8GHz and 19.35GHz, Roughness (Cao et al., 2018) at 37GHz, respectively.

Table 2: Average statistical values of the correlation results based on the BPNN training

Surface parameters	**Related percentage (dTB)**			
	3GHz	**7.8GHz**	**19.35GHz**	**37GHz**
Roughness	18.31	25.74	29.97	21.41
DTE	18.33	16.36	19.33	15.14
Slope	18.66	27.81	28.74	19.36
Aspectm	9.77	5.61	5.80	11.83
kh	19.95	9.33	20.96	18.87
kv	14.96	12.57	8.81	13.39

In this part, the statistical correlations between multichannel dTB distributions and the surface parameters are discussed to interpret what topographic features can be related to the TB variations. In other word, the correlation analysis provides a way to show how TB reflects the topographic features of the studying region.

In general, the correlations between different surface parameters are difficult to show linear relationships. Li et al. (2017) proposed a non-linear approximation called back propagation neural network (BPNN) for analyzing the topographic statistical correlation. The BPNN contains one input layer, one hidden layer, and one output layer for training the selected parameters and obtaining the correlation values (unit: %). The related matrix containing the information of the input surface parameters (roughness, DTE, Slope, Aspectm, kh, kv) are defined as:

$$M_R = \begin{bmatrix} x_{1,1} & x_{1,2} & \dots & x_{1,M} \\ x_{2,1} & x_{2,2} & \dots & x_{2,M} \\ \vdots & \vdots & \vdots & \vdots \\ x_{6,1} & x_{6,2} & \dots & x_{6,M} \end{bmatrix} \tag{12}$$

where M_R denotes the related matrix with the input surface parameters. M denotes the number of the input values contained in the study area. Each row of M_R ($[x_{i,n}|i = 1, 2, \dots, 6, m = 1, 2, \dots, M]$) contains the values of selected surface parameters. Thus, the relationship between dTB and M_R can be expressed as:

$$dTB = w_{ih} \times w_{ho} \times M_R \tag{13}$$

Through the BPNN training, the correlation weight matrix (w_{ih} and w_{ho}) can be obtained, where w_{ih} denotes the weight matrix between the input layer and the hidden layer, and w_{ho} denotes the weight matrix between the hidden layer and output layer. The correlation sequence w is defined as $w_{ih} \times w_{ho}$, where $w = [w_1, w_2, \dots, w_6]$. In this study, the input order of the surface parameters can be seen in Figure 9. Each element in sequence is related to the values in the related row of M_R. For example, w_1 denotes the correlation value between dTB and topographic roughness.

Since the statistical results of correlations are disordered (Figure 9), the averaged related percentage is calculated to indicate the differences of correlations between the multichannel dTBs and surface parameters in Table 2. At 3GHz, dTB values are affected by the subsurface materials (e.g., FTCs in Figure 7). *kh* indicates highest related percentage that can agree with this features of dTB variations, because *kh* reflects the topographic variations in the horizontal directions and high FTCs show large clusters on the subsurface (Figure 7). At 7.8GHz, the high-cratered areas and topographic bulges (see HU9 and HU11 in Figure 1), which indicate high topographic vertical variations, show high dTBs (from 11 to 12). Therefore, the highest related percentage of Slope can

agree with this result. At 19.35 and 37GHz, dTB reflects the thermal features on lunar surface, these features influence different types of geological units in the floor. These geological units are generally complex and irregular (see HU9 and HU11 in Figure 1). These complex geological units always show high topographic roughness at hectometer- and kilometer-scales (Rosenburg et al., 2011; Kreslavsky et al., 2013; Cao et al., 2015, 2018) . Therefore, the highest related percentage can statistically interpret the dTB variations at these channels.

Thus, the multichannel dTB distributions indicate more and more complex topographic variations following with the frequency increases.

5 Conclusion

In this paper, we create the dTB maps based on Chang'E-2 microwave radiometer data to improve the understanding of the geological unit divisions and formation processes of Mare Humboldtianum. Moreover, the BPNN method provides a way to analyze the relation between multichannel dTB values and the surface parameters. The main results are concluded as follows:

1. The dTB performances in Mare Humboldtianum were strongly affected by the topography. Most of the topographic effect were found in the large craters in the basin floor. The strong correlation results were also be observed by the comparison with FTC maps.
2. The basaltic units identified previously are not recognized by the dTB maps. The dTB maps indicated that there should exist two different mare activities in the eastern and western parts in the basin floor.
3. Several abnormally high dTB performances were found in the eastern part of the basin floor. These new founding indicated that most of the dTB anomalies indicated the strong correlation with the special tectonic features.
4. The BPNN method was first used to analyze the statistical relations between TB variations and the surface parameters. Multichannel TB variations reflected different topographic features. At 3GHz, different types of terrains indicated similar dTB distributions. The geological units with high elevation differences showed strong statistical correlations with dTB distributions at 7.8GHz, respectively. At 19.35and 37GHz, the dTB variations in the clusters were complex.

Acknowledgments

The authors thank Quickmap Team to provide the helpful software for analysis (available at `https://quickmap.lroc.asu.edu/`), and GMT Team for helpful software (downloaded at `https://www.generic-mapping-tools.org/`). The TB data are avialable online (at `http://moon.bao.ac.cn`). The data for roughness calculation and mapped are download from LOLA PDS Data Node (at `http://imbrium.mit.edu/`). This work was supported in part by the National Natural Science Foundation of China (No. 42071309), in part by the Science and Technology Development Fund of Macau under Grant 0052/2020/AFJ, Grant 0038/2020/A, Grant 0012/2018/A1, and Grant 0069/2018/A2, in part by the Open Fund of the State Key Laboratory of Remote Sensing Science under Grant OFSLRSS201901, in part by the Open Project Program of the State Key Laboratory of Virtual Reality Technology and Systems at Beihang University under Grant VRLAB2019C02, and in part by the grants from Guangdong Provincial College Innovative Project (No. 2018KQNCX346, No. 2018KTSCX300, and No. 2019KZDXM060).

References

Ahmadzadeh, M. R., & Petrou, M. (2001, September). Error statistics for slope and aspect when derived from interpolated data. *IEEE T. Geosci. Rmote*, *39*(9),

1823-1833. doi: 10.1109/36.950801

B. Li and X. Wang and J. Zhang and J. Chen and Z. Ling. (2016, Jun.). Lunar textural analysis based on WAC-derived kilometer-scale roughness and entropy maps. *Planet. Space Sci.*, *125*, 62-71. doi: 10.1016/j.pss.2016.03.004

Baker, D. M. H., Head, J. W., Neumann, G. A., Smith, D. E., & Zuber, M. T. (2012, March). The transition from complex craters to multi-ring basins on the Moon: Quantitative geometric properties from Lunar Reconnaissance Orbiter Lunar Orbiter Laser Altimeter (LOLA) data. *J. Geophys. Res. Planets*, *117*, E00H16. doi: 10.1029/2011JE004021

Barker, M. K., Mazarico, E., Neumann, G. A., Zuber, M. T., Haruyama, J., & Smith, D. E. (2016, July). A new lunar digital elevation model from the Lunar Orbiter Laser Altimeter and SELENE Terrain Camera. *Icarus*, *273*, 346-355. doi: 10.1016/j.icarus.2015.07.039

Booker, J. R., Kovach, R. L., & Lu, L. (1970, November). Mascons and lunar gravity. *J. Geophys. Res.*, *75*(32), 6558-6564. doi: 10.1029/JB075i032p06558

Cai, Y., & Fa, W. (2020). Meter-scale topographic roughness of the moon: The effect of small impact craters. *J. Geophys. Res. Planets*, *125*(e2020JE006429). doi: 10.1029/2020JE006429

Cao, W., & Cai, Z. (2018, July). Improved multiscale roughness algorithm for lunar surface. *IEEE J. Sel. Topics Appl. Earth Observ. Remote Sens.*, *11*(7), 2336-2345. doi: 10.1109/JSTARS.2018.2822297

Cao, W., Cai, Z., & Tang, Z. (2015, June). Fractal structure of lunar topography: An interpretation of topographic characteristics. *Geomorphology*, *238*, 112-118. doi: 10.1016/j.geomorph.2015.03.002

Cao, W., Cai, Z., & Ye, B. (2018, Mar.). Measuring multiresolution surface roughness using V-system. *IEEE Trans. Geosci. Remote Sens.*, *56*(3), 1497-1506. doi: 10.1109/TGRS.2017.2764519

Fa, W., Cai, Y. Z., & Tian, W. (2016, April). Topographic roughness of the northern high latitudes of Mercury from MESSENGER Laser Altimeter data. *Geophys. Res. Lett.*, *43*, 3078-3087. doi: 10.1002/2016GL068120

Fang, T., & Fa, W. (2014, April). High frequency thermal emission from the lunar surface and near surface temperature of the Moon from Chang'E-2 microwave radiometer. *Icarus*, *232*, 34-53. doi: 10.1016/j.icarus.2013.12.024

Fassett, C. I., Head, J. W., Kadish, S. J., Mazarico, E., Neumann, G. A., Smith, D. E., & Zuber, M. T. (2012, February). Lunar impact basins: Stratigraphy, sequence and ages from superposed impact crater populations measured from Lunar Orbiter Laser Altimeter (LOLA) data. *J. Geophys. Res. Planets*, *117*, E00H06. doi: 10.1029/2011JE003951

Feng, J., Siegler, M. A., & Hayne, P. O. (2020, January). New Constraints on Thermal and Dielectric Properties of Lunar Regolith from LRO Diviner and CE-2 Microwave Radiometer. *J. Geophys. Res-Planet*, *125*(1), e2019JE006130. doi: 10.1029/2019JE006130

Fortezzo, C. M., Spudis, P. D., & Harrel, S. L. (2020, March). Release of the digital unified global geologic map of the Moon. In *Lunar sci. conf. 51st.*

Freed, A. M., Johnson, B. C., Blair, D. M., Melosh, H. J., Neumann, G. A., Phillips, R. J., ... Zuber, M. T. (2014, September). The formation of lunar mascon basins from impact to contemporary form. *J. Geophys. Res. Planets*, *119*, 2378– 2397. doi: 10.1002/2014JE004657

Head, J. W., Fassett, C. I., Kadish, S. J., Smith, D. E., Zuber, M. T., Neumann, G. A., & Mazarico, E. (2010, September). Global distribution of large lunar craters: Implications for resurfacing and impactor populations. *Science*, *329*, 1504. doi: 10.1126/science.1195050

Hiesinger, H., & Head, J. W. (2003, July). Ages and stratigraphy of mare basalts in Oceanus Procellarum, Mare Nubium, Mare Cognitum, and Mare Insularum. *J. Geophys. Res.*, *108*(E7), 5065. doi: 10.1029/2002JE001985

Hiesinger, H., Head, J. W., Wolf, U., Jaumann, R., & Neukum, G. (2010, March). Ages and stratigraphy of lunar mare basalts in mare frigoris and other nearside maria based on crater size-frequency distribution measurements. *J. Geophys. Res.*, *115*, E03003. doi: 10.1029/2009JE003380

Hiesinger, H., Head, J. W., Wolf, U., Jaumann, R., & Neukum, G. (2011, March). Ages and stratigraphy of lunar mare basalts: A synthesis. In (Vol. 477, p. 1-51). Recent Advances and Current Research Issues in Lunar Stratigraphy. doi: 10.1130/2011.2477(01)

Hiesinger, H., Jaumann, R., Neukum, G., & Head, J. W. (2000, December). Ages of mare basalts on the lunar nearside. *J. Geophys. Res.*, *105*(E12), 29239-29275. doi: 10.1029/2000je001244

Hiesinger, H., Oberst, J., Jaumann, R., Neukum, G., & Head, J. W. (1996, March). Observations of Mare Humboldtianum: Topography, ages and multispectral characteristics. In *Lunar sci. conf. 27th* (p. 547-548). Retrieved from `https://www.lpi.usra.edu/meetings/lpsc1996/pdf/1274.pdf`

Hu, G., Chan, K., Zheng, Y., & Xu, A. (2018, September). A rock model for the cold and hot spots in the Chang'E microwave brightness temperature map. *IEEE T. Geosci. Remote.*, *56*(9), 5471-5480. doi: 10.1109/TGRS.2018.2817654

Hu, G., Zheng, Y., Xu, A., & Tang, Z. (2015, December). Microwave brightness temperature of the Moon: The possibility of setting a calibration source of the lunar surface. *IEEE Geosci. Remote S.*, *13*(2), 182-186. doi: 10.1109/LGRS.2015.2504543

Kreslavsky, M. A., & Head, J. W. (2000, November). Kilometer-scale roughness of Mars: Results from MOLA data analysis. *J. Geophys. Res.*, *105*(E11), 26695-26711. doi: https://doi.org/10.1029/2000JE001259

Kreslavsky, M. A., Head, J. W., Neumann, G. A., Rosenburg, M. A., Aharonson, O., Smith, D. E., & Zuber, M. T. (2013, September). Lunar topographic roughness maps from Lunar Orbiter Laser Altimeter (LOLA) data: Scale dependence and correlation with geologic features and units. *Icarus*, *226*(1), 52-66. doi: 10.1016/j.icarus.2013.04.027

Lan, T., & Cai, Z. (2018, December). Lunar brightness temperature map and TB distribution model. *IEEE. T. Geosci. Remote*, *6*(12), 7310-7323. doi: 10.1109/TGRS.2018.2850034

Lan, T., Cai, Z., & Ye, B. (2020, June). Modeling of lunar digital terrain entropy and terrain entropy distribution model. *IEEE T. Geosci. Remote*, 1-15. doi: 10.1109/TGRS.2020.2999582

Li, A., Cai, Z., & Cao, W. (2017, Dec.). Correlation analysis between lunar surface roughness and other land-surface parameters using BPNN. *IEEE J. Sel. Topics Appl. Earth Observ. Remote Sens.*, *10*(12), 5647-5656. doi: 10.1109/JSTARS.2017.2746899

Meng, Z., Chen, S., Wang, Y., Wang, T., Cai, Z., Zhang, Y., ... Hu, S. (2020, February). Reevaluating Mare Moscoviense and its vicinity using Chang'E-2 Microwave Sounder Data. *Remote Sens.*, *12*(535). doi: 10.3390/rs12030535

Meng, Z., Hu, S., Wang, T., Li, C., Cai, Z., & Ping, J. (2018, September). Passive microwave probing Mare Basalts in Mare Imbrium using CE-2 CELMS data. *IEEE J. Sel. Topics Appl. Earth Observ. Remote Sens.*, *11*(9), 3097-3104. doi: 10.1109/JSTARS.2018.2845417

Meng, Z., Wang, Y., Chen, S., Zheng, Y., Shi, J., Wang, T., ... Hou, L. (2019, May). MTE features of Apollo Basin and its significance in understanding the SPA Basin. *IEEE J. Sel. Topics Appl. Earth Observ. Remote Sens.*, *12*(7), 2575-2583. doi: 10.1109/JSTARS.2019.2916061

Moriarty, D. P., & Pieters, C. M. (2016, January). Complexities in pyroxene compositions derived from absorption band centers: Examples from Apollo samples, HED meteorites, synthetic pure pyroxenes, and remote sensing data. *Meteorit.*

Planet. Sci., *51*(2), 207-234. doi: 10.1111/maps.12588

Oberst, J., Wählisch, M., Zhang, W., Roatsch, T., Cook, A. C., & Jaumann, R. (1996, March). New data on lunar topography derived from Galileo and Clementine stereo images. In *Lunar sci. conf. 27th* (p. 973-974). Retrieved from `https://www.lpi.usra.edu/meetings/lpsc1996/pdf/1487.pdf`

Olaya, V. (2009). Basic land-surface parameters. In T. Hengl & H. I. Reuter (Eds.), *Geomorphometry: Concepts, Software, Applications* (Vol. 33, p. 141-169). Amsterdam, The Netherlands: Elsevier.

Rosenburg, M. A., Aharonson, O., Head, J. W., Kreslavsky, M. A., Mazarico, E., Neumann, G. A., ... Zuber, M. T. (2011, Feb.). Global surface slopes and roughness of the Moon from the Lunar Orbiter Laser Altimeter. *J. Geophys. Res.*, *116*(E02001). doi: 10.1029/2010JE003716

Shepard, M. K., Campbell, B. A., Bulmer, M. H., Farr, T. G., Gaddis, L. R., & Plaut, J. J. (2001, Dec.). The roughness of natural terrain: A planetary and remote sensing perspective. *J. Geophys. Res.*, *106*(E12), 32777-32795.

Smith, D. E., Zuber, M. T., Jackson, G. B., Cavanaugh, J. F., Neumann, G. A., Riris, H., ... Zagwodzki, T. W. (2010, May). The Lunar Orbiter Laser Altimeter Investigationon the Lunar Reconnaissance Orbiter Mission. *Space Sci. Rev.*, *150*, 209-241. doi: 10.1007/s11214-009-9512-y

Song, R., Ma, H., & Qi, D. (2007, Sep.). The complete orthogonal V-system and its applications. *Commun. Pure Appl. Anal.*, *6*(3), 853-871. doi: 10.3934/cpaa.2007.6.853

Susorney, H. C. M., Barnouin, O. S., Ernst, C. M., & Byrne, P. K. (2017, June). The surface roughness of Mercury from the Mercury Laser Altimeter: Investigating the effects of volcanism, tectonism, and impact cratering. *J. Geophys. Res. Planets*, *122*, 1372-1390. doi: 10.1002/2016JE005228

Susorney, H. C. M., Barnouin, O. S., Ernst, C. M., & Stickle, A. M. (2018, Jun.). The surface roughness of large craters on Mercury. *J. Geophys. Res. Planets*, *123*, 1581-1596. doi: 10.1029/2017JE005462

Susorney, H. C. M., Johnson, C. L., Barnouin, O. S., Daly, M. G., Seabrook, J. A., Bierhaus, E. B., & Lauretta, D. S. (2019, January). The global surface roughness of 25143 itokawa. *Icarus*, *325*, 141-152. doi: 10.1016/j.icarus.2019.01.021

Zheng, Y., Chan, K., Tsang, K., Zhu, Y., Hu, G., Blewett, D. T., & Neish, C. (2019, February). Analysis of Chang'E-2 brightness temperature data and production of high spatial resolution microwave maps of the Moon. *Icarus*, *319*, 627-644. doi: 10.1016/j.icarus.2018.09.036

Zheng, Y., Tsang, K., Chan, K., Zou, Y., Zhang, F., & Ouyang, Z. (2012, May). First microwave map of the Moon with Chang'E-1 data: the role of local time in global imaging. *Icarus*, *219*, 194-210. doi: 10.1016/j.icarus.2012.02.017

Zhu, Y., Zheng, Y., Fang, S., Zou, Y., & Pearson, S. (2019, January). Analysis of the brightness temperature features of the lunar surface using 37 GHz channel data from the Chang'E-2 microwave radiometer. *Adv. Space Res.*, *63*, 750-765. doi: 10.1016/j.asr.2018.10.014